High Thermoelectric Performance in Multi-pocketed Full-Heuslers and Their Defect Energetics

Junsoo Park,[1,*] Yi Xia,[2] Alex M. Ganose,[1] Anubhav Jain,[1,†] and Vidvuds Ozoliņš[3,4,‡]

[1] *Energy Technologies Area, Lawrence Berkeley National Laboratory, Berkeley, CA 94720, USA*
[2] *Department of Materials Science & Engineering, Northwestern University, Evanston, IL 60208, USA*
[3] *Department of Applied Physics, Yale University, New Haven, CT 06511, USA*
[4] *Energy Sciences Institute, Yale University, West Haven, CT 06516, USA*

(Dated: March 13, 2020)

This study, utilizing high-fidelity methods for computing electron-phonon scattering rates, theoretically demonstrates that ultrahigh intrinsic bulk thermoelectric performance across cryogenic-to-high temperatures is physically possible. It also demonstrates the benefit of accidental band degeneracy to thermoelectric performance is conditional upon their characters. Full-Heusler Sr_2BiAu featuring ten energy-aligned dispersive pockets (six along $\Gamma - X$ and four at L) is herein predicted to be theoretically capable of delivering $zT = 0.4 - 4.9$ at $100 - 700$ K. Relative to the previously investigated Ba_2BiAu, the additional L-pockets in Sr_2BiAu significantly increase the power factor at low temperatures, as high as 12 mW m^{-1} K^{-2} near room temperature. As temperature rises, the performance decays quickly and sinks below that of Ba_2BiAu due to the differing dispersion and scattering characteristics of the L and $\Gamma - X$ states. Sr_2SbAu is generally projected to deliver worse performance due to the appreciable energy-misalignment in the two accessible band pockets. The dominant intrinsic defect at play is Bi/Sb_{Au} antisites, which limit the n-dopabilities of all of the Heusler compounds. Calculations suggest only Sr_2SbAu potentially has both a large enough stability region and high enough Sb_{Au} antisite formation energies to retain some small chance at experimental realization as a high-performing thermoelectric.

I. INTRODUCTION

Thermoelectricity is a clean energy harvesting technology that allows direct interconversion between heat and electric current. The indicator of thermoelectric efficiency is the dimensionless figure of merit known as zT. To date, bulk thermoelectric materials have not overcome $zT = 3$, with $zT = 2$ only achieved in a few chalcogenide compounds [1–10]. Materials that deliver commercially-relevant performance below room temperature are particularly scarce, where alloys of Bi_2Te_3 [11–13] and Mg_3Sb_2-Mg_3Bi_2 [14–17] are essentially the only materials with zT near 1. This is unfortunate since many industrial applications, including refrigeration and spacecraft propulsion, would greatly benefit from efficient thermoelectrics at room-to-cryogenic temperatures [18–21].

The dearth of efficient thermoelectrics especially at low temperatures can easily be inferred from the definition $zT = \frac{\alpha^2\sigma T}{\kappa}$. Here, $\alpha^2\sigma$ is the thermoelectric power factor (PF), composed of the Seebeck coefficient (α) and electronic conductivity (σ). The total thermal conductivity (κ) is the sum of lattice thermal conductivity and electronic thermal conductivity ($\kappa_{\text{lat}} + \kappa_{\text{e}}$). A desirable thermoelectric material requires high α and σ with low κ. Unfortunately, such a combination is inherently difficult to achieve [22–27]. At low temperatures, due to small T and high κ_{lat}, designing for high PF is all the more indispensable, but unfortunately high PF is generally limited by the counterproductive behaviors of α and σ. High σ must then arise from high mobility(μ) since attempts to boost it via doping necessarily suppresses α. A large number of band pockets is generally thought to enhance σ at presumably little to no expense in α because it can deliver higher carrier concentration for given Fermi level. These considerations are best represented by bands of 1) small effective mass (m) capable of producing μ and 2) high band degeneracy or pocket multiplicity [26, 28–32].

As a culmination of these concepts, full-Heusler Ba_2BiAu (n-type) was recently studied based on a rigorous treatment of electron-phonon and phonon-phonon scattering, and has led to the prediction of an unprecedentedly high $zT \approx 5$ at 700 K and a promising $zT = 1.5$ at 300 K [33]. In this compound, one highly dispersive conduction band pocket along sixfold degenerate $\Gamma - X$ proved critical to the high PF. Meanwhile, κ_{lat} is minimal due to anharmonic rattling of Au atoms, a trait shared by this class of full-Heusler compounds [34]. The study showcased a rare coexistance of very high PF and ultralow κ_{lat} for bulk thermoelectrics — albeit without consideration of dopability and the experimental realizability of the compound.

In the present work, we achieve the following. 1) We show that analogous but multi-pocketed full-Heusler compounds, in particular Sr_2BiAu, can theoretically attain even higher thermoelectric performance across a broader temperature spectrum, which is especially niche at low temperatures. 2) We analyze the benefit of pocket multiplicity in the form of accidental (non-symmetry-related) degeneracy, which we conclude is conditional upon the similarities of the pockets. 3) By investigating phase stability and intrinsic defects, we predict that

* jsyony37@ucla.edu
† ajain@lbl.gov
‡ vidvuds.ozolins@yale.edu

due to the formation of Bi/Sb_{Au} antisite formations, the Heusler compounds stand slim chance of being realized as high-performing thermoelectrics, though Sr_2SbAu might fare better than the rest.

II. COMPUTATIONAL METHODS

A. Electronic Structures

The electronic structure is calculated with Quantum Espresso [35, 36] with the Optimized Norm-Conserving Vanderbilt pseudopotentials [37–39] and Perdew-Burke-Ernzerhof (PBE) exchange-correlation functional [40] with and without spin-orbit coupling (SOC) for comparisons. Plane-wave cutoff of 100 Ry is used. In order to obtain more accurate band gaps, advanced functionals such as Becke-Johnson potential by Tran and Blaha (mBJ) [41] and the Heyd-Scuseria-Ernzerhof hybrid-exchange functional (HSE06) [42, 43] were used. Band analysis was done on sumo [**?**].

B. Electron-phonon Scattering

In treating electron-phonon scattering, we first compute electronic states and e-ph interaction matrix elements at a coarse $8 \times 8 \times 8$ **k**-point mesh, using phonon perturbations computed at a coarse $4\times4\times4$ **q**-point mesh using density functional perturbation theory (DFPT) [44, 45]. Then with the EPW package [46–49] we interpolate electronic states, phonons, and the matrix elements onto dense $40 \times 40 \times 40$ **k**-point and **q**-point meshes through maximally localized Wannier functions [50–52]. Long-ranged polar optical scattering matrix elements are added on the dense **k**-mesh [53]. The imaginary part of the resulting electron self-energy leads directly to band-and-**k**-dependent electron lifetimes ($\tau_{\nu\mathbf{k}}$) limited by electron-phonon (e-ph) scattering. Supplemental Material [54] has further theoretical details.

C. Electron Transport

With $\tau_{\nu\mathbf{k}}$ as inputs, we employ the Boltzmann transport formalism (implemented in BoltzTraP [55] modified in-house) in the relaxation time approximation (RTA) to compute electron transport properties:

$$\sigma = \frac{1}{\Omega N_{\mathbf{k}}} \sum_{\nu\mathbf{k}} (\tau v^2)_{\nu\mathbf{k}} \left(-\frac{\partial f}{\partial E}\right)_{\nu\mathbf{k}}, \tag{1}$$

$$\alpha = \frac{\sigma^{-1}}{\Omega T N_{\mathbf{k}}} \sum_{\nu\mathbf{k}} (\tau v^2)_{\nu\mathbf{k}} (E_{\mathrm{F}} - E_{\nu\mathbf{k}}) \left(-\frac{\partial f}{\partial E}\right)_{\nu\mathbf{k}}, \tag{2}$$

$$\kappa_e = \frac{1}{\Omega T N_{\mathbf{k}}} \sum_{\nu\mathbf{k}} (\tau v^2)_{\nu\mathbf{k}} (E_{\mathrm{F}} - E_{\nu\mathbf{k}})^2 \left(-\frac{\partial f}{\partial E}\right)_{\nu\mathbf{k}} - \alpha^2 \sigma T. \tag{3}$$

The validity of RTA coupled with e-ph matrix elements calculated via DFPT and Wannier interpolation has been well-established by multiple recent instances of application that approximated experimental measurements well [56–59]. In performing Eqs. 1–3 we utilize the band structure calculated with SOC and the band gap value from mBJ+SOC for consistent comparison with our previous study on Ba_2BiAu. For Sr_2BiAu, since the effect of SOC on the electronic structure or phonon is minimal (as will be shown), SOC is neglected for the computations of electron-phonon scattering, due to the computational expense. For Sr_2SbAu, however, SOC substantially impacts the electronic structure and is therefore included in electron-phonon scattering computations.

D. Stability and Defects

We use Vienna *Ab initio* Simulations Package (VASP) [64–67] throughout this section to perform DFT total energy calculations for both competing phases and defective supercells. We also incorporate SOC and use the projector-augmented wave (PAW) pseudopotentials [68] with the PBE functional throughout.

All binary and ternary phases that could potentially form from the compositions of the Heuslers compounds available on Materials Project [60] and Inorganic Crystal Structure Database [61–63] are considered for the evaluation of phase stability. Sr_2BiAu has thirteen competing binary and ternary phases, while Ba_2BiAu has ten, Sr_2SbAu twelve, and Ba_2SbAu fifteen. We construct the ternary phase diagrams using the calculated formation energies (shown in Fig. S4 of Supplemental Material [54]), which reveal the phase fields under each of which various pairs of competing phases may coexist with the compounds of interest. The equilibrium chemical potentials are derived using the corresponding phase fields. Of note, all compounds with energies within the numerical noise of DFT ($\sim$10 meV per atom) from the convex hull were placed on the hull.

We consider all possible vacancy and antisite intrinsic point defects, and employ the standard supercell approach. We create host and defective supercells that are $2 \times 2 \times 2$ expansions of the fully relaxed conventional cubic unit cells of the compounds. The host supercells contain 128 atoms, of which 64 are Ba/Sr atoms, 32 are Bi/Sb atoms, and 32 are Au atoms. This is allowed for all types of point defects because a full-Heusler crystal structure remains identical upon the exchange of lattice sites between the Ba/Sr atoms and the Bi/Sb and Au atoms. For charged supercells, electrons are either removed or added according to the charge. For total energies of defective supercells, a plane-wave cut-off energy of 600 eV and a $2\times2\times2$ **k**-point mesh are used throughout all self-consistent calculations of defective supercells. All

relaxations are performed with the Methfessel-Paxton's smearing scheme [69] to properly treat the metallic characteristics of the cells with charged defects.

Point defect formation energies are calculated as

$$\Delta E_f^{\mathrm{D}} = E^{\mathrm{D}} - E^{\mathrm{Host}} - \sum_a \Delta N_a \mu_a + q(E_v + E_{\mathrm{F}}) + E_{\mathrm{cor}}, \quad (4)$$

where E^{D} is the total energy of a defective cell, E^{Host} is the total energy of a host full-Heusler cell into which a defect is introduced, q is the charge on the defect and μ_a is the chemical potential of element a in the compounds (e.g., as determined by the phase diagram). ΔN_a is the excess (positive) or deficient (negative) number of atoms of element a in the defective cell relative to the host cell. For instance, if the defect is an $\mathrm{Bi_{Au}}$ antisite (Bi in place of Au), then $\Delta N_{\mathrm{Bi}} = 1$ and $\Delta N_{\mathrm{Au}} = -1$. E_{F} is a free parameter and represents the Fermi level as counted positively up from E_v, which is the energy required to remove an electron from a given host, i. e., the valence band maximum (VBM) of the host compound. Lastly, E_{cor} is a correction term for finite-sized supercells, which experience several fictitious effects.

Charged defects experience experience fictitious electrostatic interactions between periodic images of the defect, due to periodic boundary condition, and interactions between the defect and the homogeneous, jellium-like background charge that enforces overall charge-neutrality. These are corrected by the method of Makov and Payne [70],

$$E_{\mathrm{cor}} = \frac{q^2\gamma}{2\epsilon L} - \frac{2\pi q Q}{3\epsilon L^3}, \quad (5)$$

where γ is the Madelung constant, Q is the quadrupole moment, L is the supercell lattice parameter, and ϵ is the dielectric constant of the host compound. While more sophisticated correction schemes have been proposed [71–73], we do not employ them because 1) the compounds have high dielectric constants, 2) cell sizes used are large enough for Eq. 5 to be acceptable ($L > 16$ Å), and 3) other methods will likely not change the main conclusions we draw. Band-gap correction also must be performed to reference the defect energies to more realistic band edges of the host compounds, for which we use HSE06 with SOC. This treatment scheme of choice is based on HSE06's credible track record of preserving the band-edge-relative defect energies calculated with PBE when aligned to a common reference level (achieved with the local electrostatic potential) [74–78]. Potential adjustment of the electrostatic reference energy between the two cells are also made. Finally, band-filling corrections [73] are also calculated, but are zero for all compounds. This set of corrections was confirmed with the aide code (not yet published). Additional details on calculations of phase stability and defect energies are provided in the Supplementary Material [54].

III. ELECTRONIC PROPERTIES

A. The Electronic Structure

The band structures of Sr_2BiAu and Sr_2SbAu are shown in 1a–b. Sr_2BiAu and Sr_2SbAu feature additional dispersive conduction band pockets at the fourfold degenerate L-point while retaining the sixfold degenerate pocket along $\Gamma - X$. SOC does not affect the conduction band pocket along $\Gamma - X$, just as in the case of Ba_2BiAu. The corresponding energy surfaces as seen in Fig. 1c reveal all ten pockets. Whereas the L-pocket of Sr_2BiAu is nearly energy-aligned with the $\Gamma - X$-pocket, the L-pocket of Sr_2SbAu is lower than the $\Gamma - X$-pocket by 0.06 eV. The effective masses of the very dispersive $\Gamma - X$-pocket are essentially identical for all three com-

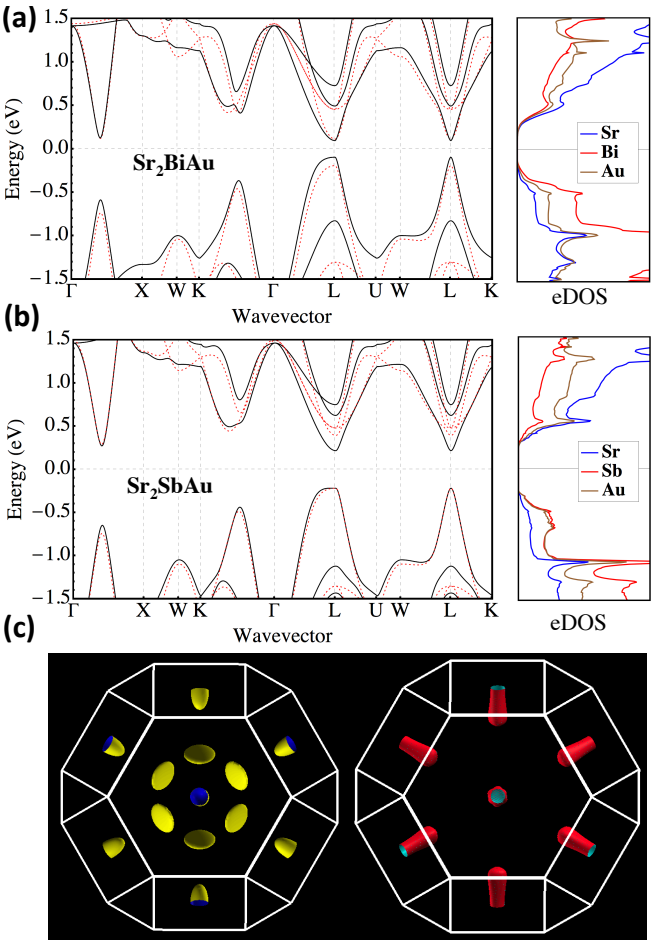

FIG. 1. (Color online) **a)** Electronic band structures of Sr_2BiAu with (black, solid) and without (red, dotted) SOC, aligned at the CBM. The atom-decomposed density of states with SOC is shown on the right. **b)** Same for Sr_2SbAu. **c)** Isoenergy surfaces of Sr_2SbAu with SOC, at 0.1 eV above the CBM (left) and below the VBM (right). The levels correspond to electron doping concentration of $n_e = 1.44 \times 10^{20}$ cm^{-3} and hole doping concentration of $n_h = 1.40 \times 10^{20}$ cm^{-3}, respectively.

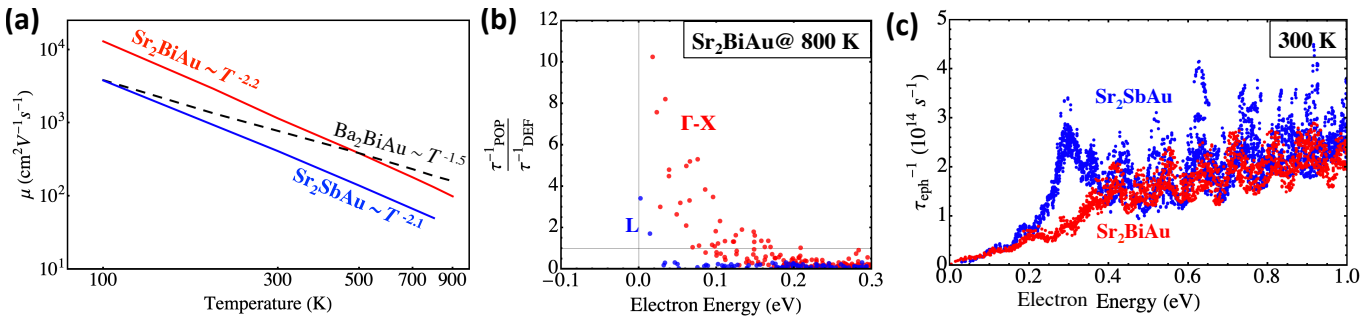

FIG. 2. (Color online) **a)** Comparison of electron mobilities of the Heusler compounds at low and high temperatures. **b)** The relative strength of polar-optical scattering (POP) and lattice deformation scattering (DEF) of the $\Gamma - X$-pocket (red), which is clearly dominated by POP, and the L-pocket (blue) which is heavily affected by DEF. **c)** Relative e-ph scattering rates of Sr_2BiAu and Sr_2SbAu at 300 K.

pounds at approximately $m_\parallel = 0.07$ and $m_\perp = 0.48$. The L-pockets are somewhat less dispersive, and their principal effective masses are approximately $m_\parallel = 0.19$ and $m_\perp = 0.45$ for both of the Sr-compounds.

A popular index for correlating a band structure to the PF it generates is the so-called Fermi surface complexity factor, calculated as [31]

$$C = N_{\text{pocket}} \left(\frac{2}{3} \left(\frac{m_\perp}{m_\parallel} \right)^{\frac{1}{3}} + \frac{1}{3} \left(\frac{m_\perp}{m_\parallel} \right)^{-\frac{2}{3}} \right)^{3/2}, \quad (6)$$

The band characters as described above yield complexity factors of 9.5 for Ba_2BiAu, which only has a $\Gamma - X$-pocket, and 14 for the two Sr-compounds, though the value is ambiguous for Sr_2SbAu where the pockets are misaligned.

The band gaps as calculated by PBE+SOC are 0.19 eV for Sr_2BiAu and 0.5 eV for Sr_2SbAu, which are severe underestimations. The mBJ functional with SOC yields 0.53 eV Sr_2BiAu and 0.85 eV for Sr_2SbAu, where HSE06 with SOC yields 0.53 eV and 0.81 eV, respectively.

B. Scattering & Mobility

Electron mobilities of the three Heusler compounds, calculated using band-and-**k**-dependent electron-phonon lifetimes, are juxtaposed in Fig. 2a. Electron mobilities of the two Sr compounds decay at a faster rate with temperature than that of Ba_2BiAu. This is due to the extra pocket L-pocket that the Sr compounds have. The L-pocket is overall heavier than the $\Gamma - X$-pocket and attains a larger electronic density of states (eDOS). Whereas the $\Gamma - X$-pocket is dispersive enough that the phase space for lattice deformation scattering is small, allowing polar-optical scattering to dominate, the heavier L-pocket is much more affected by deformation scattering [see Fig. 2c]. It is well known that lattice deformation results in quicker temperature-decay of mobility than polar-optical interactions. Therefore, presence of the L-states result in faster decay of mobility with temperature than if only the $\Gamma - X$-pocket were present, which in turn results in quicker decay of mobilities of the Sr compounds than that of Ba_2BiAu.

Though the mobilities of the Sr compounds exhibit similar trends, they notably differ in magnitude. This is partially due to the fact that the heavier L-pocket is the true band minimum in Sr_2SbAu, whereas in Sr_2BiAu it is nearly perfectly aligned with the $\Gamma - X$-pocket. Sr_2SbAu also generally experiences somewhat heavier scattering especially around 0.3 eV above the CBM, as seen in Fig. 2c. The differences in the temperature-dependence of mobility arising from accidentally degenerate pockets that are disparate in character translate to the behavior of their thermoelectric properties of the compounds, as will be seen.

We find that there is little to no intervalley scattering between the two pockets. When we artificially remove the L-pockets such that their participation to scattering of other states is forbidden, we detect virtually no change in the scattering rates of the remaining $\Gamma - X$-pocket.

IV. THERMOELECTRIC PROPERTIES

A. The Power Factor

Sr_2BiAu is capable of attaining very high n-type PFs across all temperatures, as shown in Fig. 3a, topping out at 12 mW m^{-1}K^{-2} near room temperature. Sr_2SbAu simply performs worse, as made clear by Fig. 3b. It is a well-known engineering strategy to boost the PF to engineer bands of multiple pockets for energy convergence [81, 82]. In essence Sr_2BiAu is a natural realization of this concept. Its theoretical PF hovers above the measured PF of the p-type NbFeSb [79] across all temperature domains [see Fig. 3c]. In contrast, Sr_2SbAu falls short of such natural band convergence as the heavier L-pocket is lower than the $\Gamma - X$-pocket by 0.06 eV. This, together with somewhat heavier scattering in Sr_2SbAu, results in both lower σ and α in comparison to Sr_2BiAu [see Fig. 3d.]

Comparison of Sr_2BiAu and Ba_2BiAu provides insights

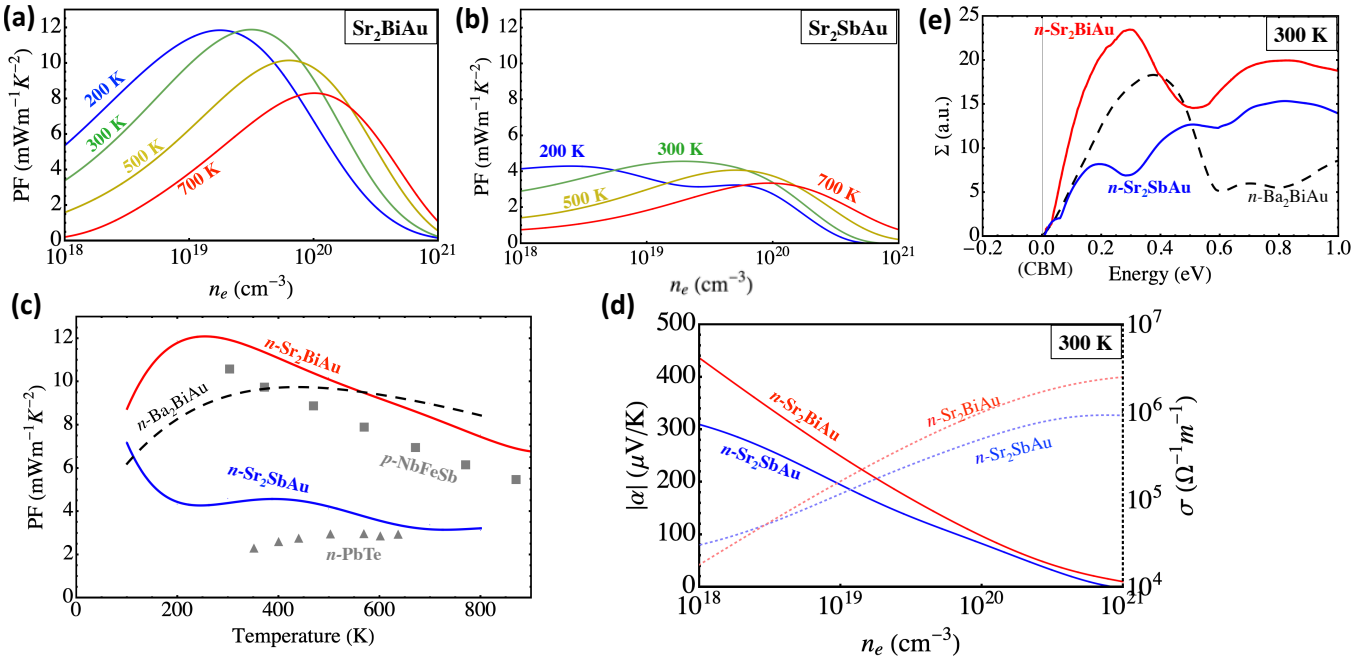

FIG. 3. (Color online) The n-type power factor of **a)** Sr_2BiAu and **b)** Sr_2SbAu against electron doping concentration. **c)** Maximum n-type power factors of Sr_2BiAu and Sr_2BiAu at each temperature juxtaposed with power factors of high-performing thermoelectrics: p-type NbFeSb [79], n-type PbTe [80], and theoretical n-type Ba_2BiAu [33]). **d)** Comparison of the n-type Seebeck coefficient (solid) and conductivity (dotted) of Sr_2BiAu (red) and Sr_2SbAu (blue) at 300 K. **e)** The spectral conductivities of three full-Heusler compounds at 300 K, where they are all zero-aligned to their respective CBMs.

to the effects of the additional, heavier L-pocket and the aforementioned temperature-dependent mobility profiles. At low temperatures, the PFs behave as expected from the complexity factors, and Sr_2BiAu easily performs better than Ba_2BiAu. However as higher temperatures excite deeper L states whose lifetimes decay quickly with energy (as reflected by mobilties), Ba_2BiAu begins to outperform Sr_2BiAu. Such a crossover indicates that the presence of a heavier pocket ultimately benefits the PF below a certain threshold temperature beyond which the deep heavy states with short lifetimes are critically excited, negating the benefit of higher carrier concentration (per Fermi level). The threshold temperature is, in turn, dependent upon the extent to which the second pocket is heavier than the first.

The essence of the overall relationship between the three band structures and their thermoelectric performance is represented by their energy-dependent spectral conductivities, $\Sigma(E) = N(E)\tau(E)v^2(E)$, plotted in Fig. 3e. In comparison to Ba_2BiAu, Sr_2BiAu attains noticeably steeper slope and higher values of $\Sigma(E)$ at its CBM due to simultaneous excitation of the $\Gamma - X$-and-L-pockets. High $\Sigma(E)$ with steep onset is an undoubted signature for both high α and σ. Meanwhile, the profile for Sr_2SbAu is kinked: the main incline corresponding to the $\Gamma - X$-pocket occurs 0.06 eV into the CBM followed by a much more gradual onset corresponding to the heavier L-pocket. This is clearly less effective for thermoelectricity.

The main lesson of the above discussions is that a multitude of inherently distinct, symmetry-inequivalent pockets of accidental degeneracy is not necessarily beneficial for thermoelectrics. It better benefits thermoelectric performance if the pockets share similar dispersion and scattering behaviors. If sufficiently different in character, then one may be better off without the heavier pocket as the disparity in pocket lifetimes and mobilities would overpower increased carrier population. Only in the perfectly symmetry-identical cases do more pockets universally lead to higher performance. More generally, this demonstrates that indicators such as the complexity factor are valid in so far as all pockets share similar if not symmetry-identical profiles in not only the band shapes but also scattering behaviors. The complexity factor becomes an increasingly poorer measure of thermoelectric performance as the band pockets are accidentally degenerate and become more disparate in character.

B. Thermal Properties and the Figure of Merit

The Lorenz numbers (L) of the Sr-based compounds are consistently below the free-electron Wiedemann-Franz value ($L_{\mathrm{WF}} = 2.44 \times 10^{-8}$ $\mathrm{W\Omega K^{-2}}$). $L < L_{\mathrm{WF}}$ by itself is expected as it reflects transport dominated by phonon scattering, whether due to polar-optical or lattice deformation [85]. Yet upon a closer examination, a couple of anomalies are spotted. L in these two com-

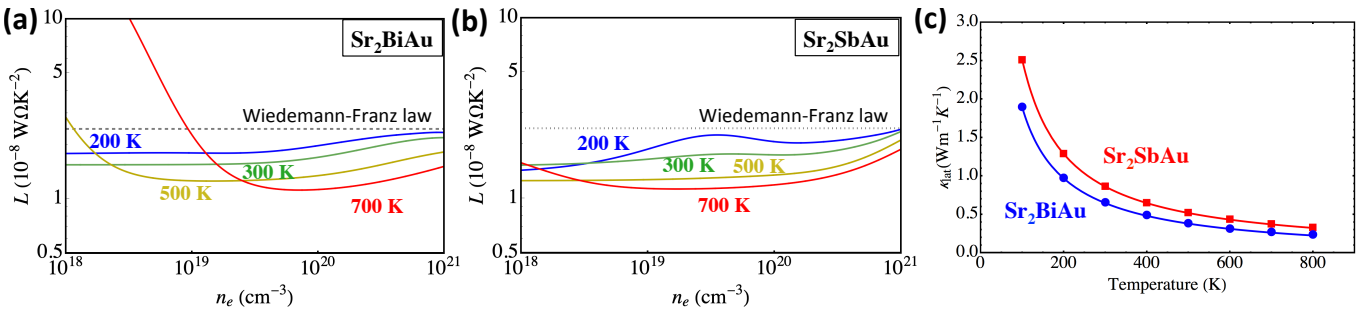

FIG. 4. (Color online) **a)** The Lorenz number of Sr_2BiAu against n-doping concentration. **b)** The Lorenz number of Sr_2SbAu against the Fermi level. The dotted horizontal lines mark the Wiedemann-Franz value. **c)** Lattice thermal conductivities of Sr_2BiAu and Sr_2SbAu.

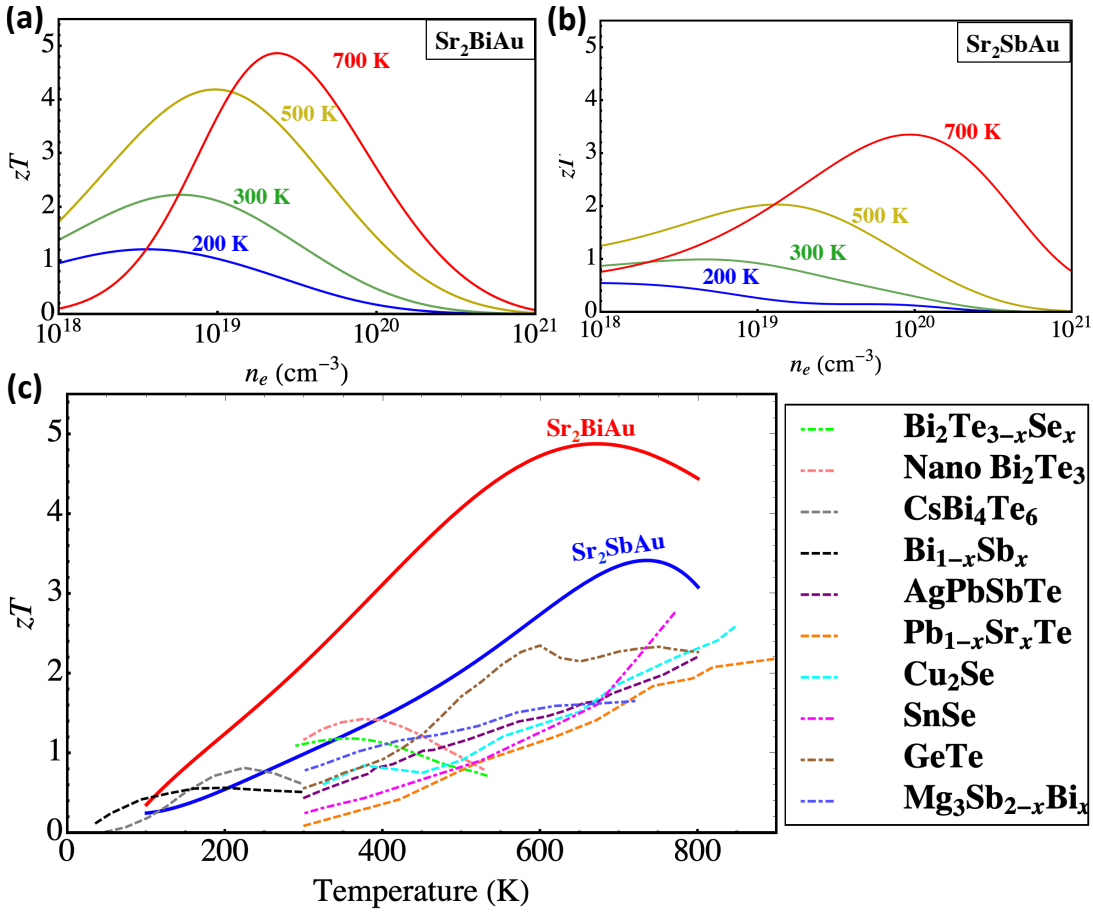

FIG. 5. (Color online) Theoretical n-type zT of **a)** Sr_2BiAu and **b)** Sr_2SbAu against electron doping concentration. **c)** Theoretical *maximum* zT of n-type Sr_2BiAu and Sr_2SbAu at each temperature in comparison to state-of-the-art thermoelectrics [1, 4, 6, 8, 10–13, 15, 16, 83, 84]

pounds decrease with temperature whereas the free electron picture predicts increasing L (towards L_{WF} with temperature [85]). Moreover, L reaches as low as 10^{-8} $\mathrm{W\Omega K^{-2}}$ if not lower at high temperatures for Sr_2BiAu. We attribute these results to the rapid rate at which scattering rates increase as the dominant process shifts from polar-optical near the band edge to lattice deformation in the deep electronic states. Referring back to Fig. 3e, at about 0.35 eV above the CBMs, $\Sigma(E)$ substantially drops in magnitude after a peak, which is associated with the spike in the scattering rate and eDOS there. Because high-energy electrons occupying deep states contribute much more to κ_e whereas low-energy electrons contribute more to σ, comparatively faster decay lifetimes at high energies, which are increasingly excited at higher temperatures, leads to lower L than if just one scattering

mechanism took place.

The small magnitudes of L and therefore κ_e relative to σ are particularly important because $\kappa_e > \kappa_{\rm lat}$ in these compounds. The ultralow $\kappa_{\rm lat}$ has been predicted by a previous study [34], whose results we reproduce here [see Fig. 4c] using the same computational methods combining compressive sensing lattice dynamics [86] and iterative Boltzmann transport [87]. Phonon dispersion and density of states can be found in the Supplemental Material [54].

The combination of high PF, and low $\kappa_{\rm lat}$ and L result in ultrahigh intrinsic zT from cryogenic to high temperatures, especially for Sr_2BiAu. Notable in particular is the high performance $zT = 0.4 - 2.2$ in the $100 - 300$ K range, which if realized would fill in the niche at low temperatures. Comparisons made in Fig. 5c reveal that the theoretical performance of Sr_2BiAu is record-high at nearly all temperatures for bulk materials. While somewhat lower in zT, Sr_2SbAu is still poised to offer higher efficiencies than most of state-of-the-art thermoelectric compounds. If the offset $\Gamma - X$-and-L-pockets could be made to align in energy via doping or temperature effect, it would attain even higher PF and zT. Overall, because κ_e is the dominant thermal conductivity and L is rather constant, zT peaks at lower $E_{\rm F}$ (n_e) than the PF where the high Seebeck coefficient develops. In fact, Fig. 5b demonstrates that zT peaks at a non-degenerate level at high temperatures. This in turn has an important consequence to n-dopability of these compounds as intrinsic defects will be shown severely constrain the amount of extrinsic electrons that can be introduced.

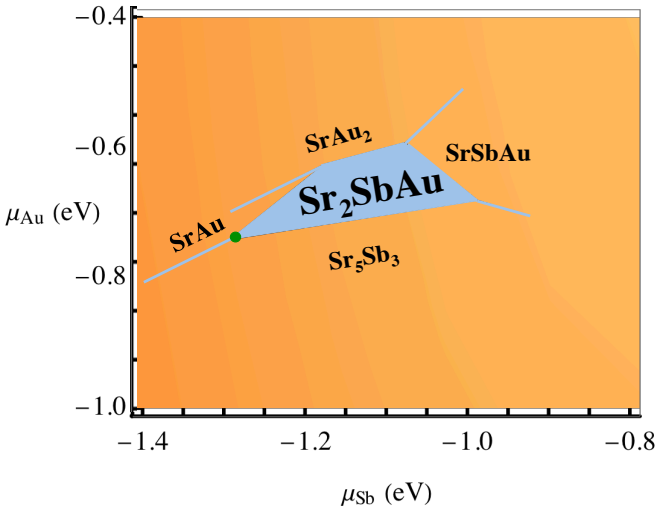

FIG. 6. (Color online) The region of phase stability (shaded red) of Sr_2SbAu in the chemical potential space of Sb (the horizontal axes), and Au (the vertical axes). The Sr chemical potential is determined by the two. Secondary competing phases to be found in the vicinity are labeled. The green dot indicates the point where the Sb_{Au} antisite has the highest formation energy and thus is least detrimental to n-doping.

V. STABILITY, DEFECTS, AND DOPABILITY

For the Heusler compounds hereby studied to experimentally realize their thermoelectric potentials, they ought to have a large region of stability and be n-dopable – desirably to their ideal carrier concentrations of $n_e \approx 10^{19}$ cm^{-3}. With the rapid emergence of computationally discovered hypothetical materials, it is important that analyses of realizability accompany performance predictions for a better guidance to experimentalists [88]. Accordingly we analyze the stability and intrinsic defect energetics of the four full-Heusler compounds (Ba_2SbAu in addition to the three compounds studied above).

A. Phase Stability

The two Sr-compounds each have a stoichiometrically identical $P21/m$ phase, as noted in a previous publication [34]. As per our PBE+SOC total energy calculation, these phases are nearly energy-equivalent with the Heusler counterparts, differing by approximately 5 meV per atom, which is beyond the numerical resolution of DFT. This indicates that either phase has a chance of forming at finite temperatures depending on the free energies and entropic contributions.

We find that Sr_2BiAu, Ba_2BiAu, and Ba_2SbAu are barely thermodynamically stable, having extremely limited regions (essentially single points) of phase stability in the chemical potential space, an unfavorable sign for synthesis. Their points of stability are $\mu_{\rm Sr} \approx -0.94$ eV, $\mu_{\rm Bi} \approx -0.81$ eV, and $\mu_{\rm Au} \approx -0.63$ for Sr_2BiAu, and $\mu_{\rm Ba} \approx -0.67$ eV, $\mu_{\rm Bi} \approx -1.26$ eV, and $\mu_{\rm Au} \approx -0.75$ for Ba_2BiAu, and $\mu_{\rm Ba} \approx -0.70$ eV, $\mu_{\rm Sb} \approx -1.49$ eV, and $\mu_{\rm Au} \approx -0.73$ for Ba_2SbAu. Sr_2SbAu is the only compound that may have a large region of phase stability as shown in Fig. 6 provided that its precise free energy is lower than that of the $P21/m$ phase at finite tem-

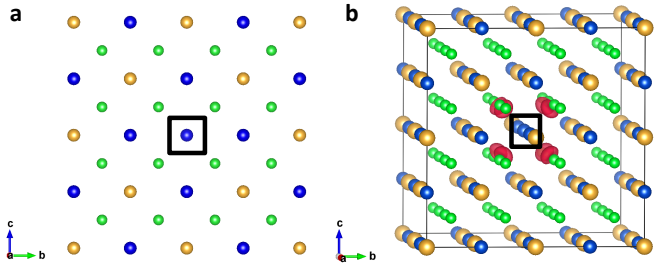

FIG. 7. (Color online) **a)** An example of defective $2 \times 2 \times 2$ supercell with a Ba/Sr_{Au} antisite on a supercell's (2 0 0) lattice plane. The location of the defect is highlighted with black squares. Ba/Sr atoms are in green, Bi/Sb atoms are in blue, and Au atoms are in, well, gold. **b)** Charge-density-difference between $q = -2$ and $q = 0$ supercells of Sr_2SbAu, where the extra negative charge (colored red) is distributed predominantly to the Sr atoms surrounding the Sb_{Au} antisite.

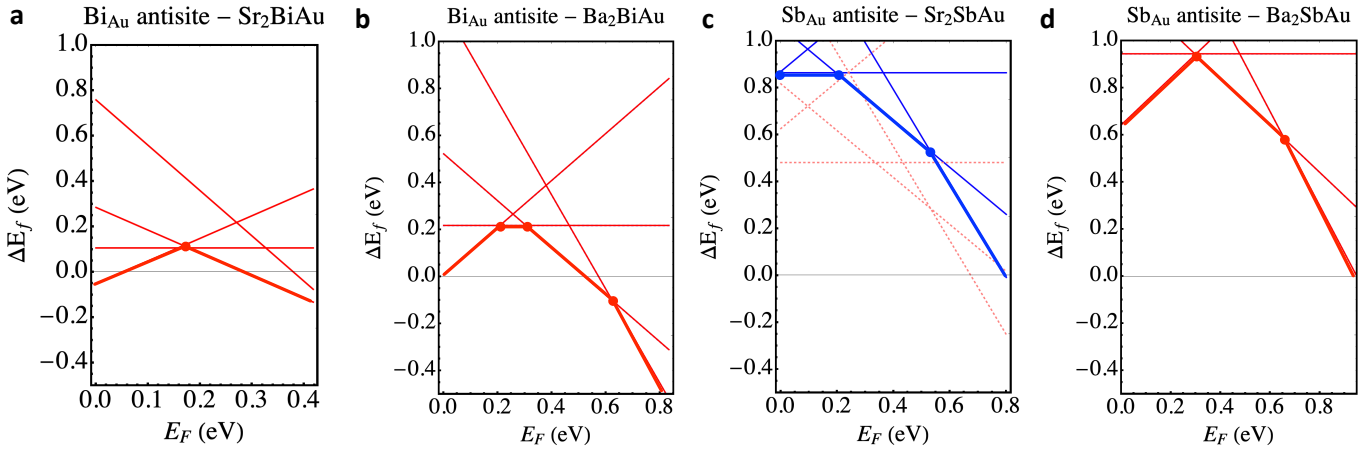

FIG. 8. (Color online) The formation energies of Bi/Sr$_{Au}$. The slopes of the lines indicate charge ($q = -2 - +1$). The plots go from the VBM (0 eV) to the CBM as determined by HSE+SOC. For Sr_2SbAu, which has a large chemical-potential region of phase stability, the Sb-and-Au-poor condition (solid blue lines) and the Sb-rich condition (dotted pink lines) are both shown. The former condition must be targeted since it leads to higher Sb$_{Au}$ defect formation energies.

peratures. Therefore, synthesis of Sr_2SbAu pure phase looks to be more probable at least compared to the other three. It is worth mentioning that a $P6_3mmc$ phase of 1:1:1 stoichiometry have been experimentally observed [89], which may serve as a starting point for tuning the chemical potentials.

B. Defects

Schematics of a supercell with a defect at the cell center are shown in Fig. 7. The small magnitudes of the correction term E_{cor} (less than 0.1 eV for the charged defects) reflect that high ϵ of the compounds inhibit strong electrostatic interactions between charged defects and their periodic images, validating the overall size-sufficiency of the supercells used.

In all four compounds, all but one type of antisite defect (see next paragraph) have high enough formation energies that they are irrelevant. All other antisite defect formations require at least 1.5 eV. All vacancies formations require at least 3 eV. One trend to note is that the defects involving Au are comparatively lower in formation energy than those that do not. This likely reflects that, at their sites, Au atoms are very weakly bonded in both compounds. After all, the weakly bonded nature of Au and its vibrational independence is precisely the phenomenon that leads to strong anharmonicity and ultralow lattice thermal conductivity in the two compounds.

By far the most energetically favored defect in all four compounds is the Bi$_{Au}$ or Sb$_{Au}$ antisite defects, whose formation energies are shown in Fig. 8. The charge-neutral defect formation energy is $0.1 - 0.2$ eV in the Bi-compounds, though considerably higher at $0.7 - 0.9$ eV in the Sb-compounds. The higher formation energies in the Sb-compounds may arise from the size mismatch between Sb and Au atoms, whereas Bi atoms are closer in size to Au atoms. Typically, the pnictogen atoms may accept up to three electrons whereas Au accepts one, for a surplus of two.

Unfortunately, the Bi$_{Au}$ and Sb$_{Au}$ antisites have severe consequences for n-dopability of the Heusler compounds. Near the CBM, these defects favor negatively charged states and hence are predicted to act as electron traps (acceptors), significantly hampering n-doping. The situation is particularly dire for Sr_2BiAu and Ba_2BiAu [see Figs. 8a–b], where these antisite defects exhibit strongly negative formation energies well below the CBM. Therefore, we determine that n-doping of the two Bi-compounds is unlikely due to Bi$_{Au}$ compensating defects.

On a brighter side, doping the Sb-compounds maybe somewhat more achievable due to the considerably higher formation energies of Sb$_{Au}$ antisites. Though they are still deep defects, $\Delta E_f^{Sb_{Au}}$ reaches 0 eV only near the HSE CBM in the Sb-and-Au-poor condition [see Figs. 8c–d]. A rough estimation of the Sb$_{Au}$ concentration at 0.15 eV below the HSE CBM and at 300 K is $\approx 10^{19}$ cm^{-3}, about the same as the optimal electron concentration of $n_e \approx 10^{19}$ cm^{-3} [see Fig. 5]. Under this estimate, roughly twice as much as n-dopant must be introduced to counter the intrinsic Sb$_{Au}$ defects. Finally, because the formation energy further decreases and n-dopability irreparably damaged under the Sb-and-Au-rich condition, it is critical that Sr_2SbAu is synthesized in the Sb-and-Au-poor condition.

All things considered, while still not optimistic, n-type Sr_2SbAu may stand a chance at realization since 1) the optimum Fermi level for zT is appreciably below the CBM for low doping, 2) the exact band gap and band edge positions may still differ from the HSE+SOC values, 3) temperature-effects such as phononic (vibrational) contributions to the solubilities of defects and

dopants are left unaccounted for, and 4) Sr_2SbAu will likely have by far the largest chemical-potential region of phase stability, as long as the formation $P21/m$ polymorph can be suppressed.

VI. CONCLUSION

In summary, the full-Heuslers in this study - especially Sr_2BiAu - constitute a theoretical validation that very high *intrinsic* thermoelectric performance across a broad range of temperatures from $100 \sim 1000$ K is physically possible in real bulk compounds. The predicted zT values are notably high at cryogenic-to-room temperatures – the domain that generally lacks efficient thermoelectric materials. Dispersive conduction band pockets at two off-symmetry points (for a total of ten pockets in the Brillouin zone) generate very high power factors across all temperatures. However, due to the disparity in the characters of the two pockets in terms of dispersion and dominant scattering mechanisms, performance decays more quickly with temperature. Whether accidentally degenerate pockets benefit thermoelectric performance is therefore conditional upon the similarity of the pockets and temperature of operation. If the pockets are too dissimilar, then performance would benefit if the lighter pocket were alone without the heavier pocket.

In spite of the high predicted thermoelectric performances, we determine that realization of n-type Sr_2BiAu and Ba_2BiAu is extremely unlikely if not impossible. They are very limited in stability with respect to chemical potentials (albeit within the limits of 0 K DFT energetics, with no accounting for phononic effects) and extremely vulnerable to formation of negatively-charged Bi/Sb_{Au} antisite defects. The antisites have very low formation energies, naturally drive the compounds to be p-type, and would function as potent electron traps near the CBM, compensating any n-doping. The Sb-compounds fare better on the the antisite defects. Sr_2SbAu appears least pessimistic due to the potentially much more sizable region of stability and comparatively high Sb_{Au} formation energies.

ACKNOWLEDGMENTS

The study was conceived and designed on National Science Foundation (NSF) Grant DMR-1611507, which funded V. O. The study was further developed and completed on the grant from U.S. Department of Energy, Office of Basic Energy Sciences, Early Career Research Program, which funded J. P., A. G., and A. J. This research used computational resources of 1) the National Energy Research Scientific Computing Center (NERSC), a DOE Office of Science User Facility supported by the Office of Science of the U.S. Department of Energy under Contract No. DE-AC02-05CH11231, and 2) Texas Advanced Computing Center (TACC) at the University of Texas at Austin through the Extreme Science and Engineering Discovery Environment (XSEDE), which is supported by NSF grant number ACI-1548562.

[1] A. A. Olvera, N. A. Moroz, P. Sahoo, P. Ren, T. P. Bailey, A. A. Page, C. Uher, and P. F. P. Poudeu, "Partial indium solubility induces chemical stability and colossal thermoelectric figure of merit in cu2se," Energy Environ. Sci.. **10**, 1668–1676 (2017).

[2] B. Zhong, Y. Zhang, W. Li, Z. Chen, J. Cui, W. Li, Y. Xie, Q. Hao, and Q. He, "High superionic conduction arising from aligned large lamellae and large figure of merit in bulk $cu_{1.94}al_{0.02}se$," Appl. Phys. Lett. **105**, 123902 (2014).

[3] L. Zhao, G. Tan, S. Hao, J. He, Y. Pei, H. Chi, H. Wang, S. Gong, H. Xu, V. Dravid, C. Uher, G. J. Snyder, C. Wolverton, and M. G. Kanatzidis, "Ultrahigh power factor and thermoelectric performance in hole-doped single-crystal snse," Science **351**, 141–144 (2016).

[4] C. Chang, M. Wu, D. He, Y. Pei, C.-F. Wu, X. Wu, H. Yu, F. Zhu, K. Wang, Y. Chen, L. Huang, J.-F. Li, J. He, and L.-D. Zhao, "3d charge and 2d phonon transports leading to high out-of-plane zt in n-type snse crystals," Science **360**, 778–783 (2018).

[5] A. T. Duong, V. Q. Nguyen, G. Duvjir, V. T. Duong, S. Kwon, J. Y. Song, J. K. Lee, J. E. Lee, S. Park, T. Min, J. Lee, J. Kim, and S. Cho, "Achieving $zt = 2.2$ with bi-doped n-type snse single crystals," Nat. Commun. **7** (2016).

[6] K. F. Hsu, S. Loo, F. Guo, W. Chen, J. S. Dyck, C. Uher, T. Hogan, E. K. Polychroniadis, and M. G. Kanatzidis, "Cubic $agpb_msbte_{2+m}$: Bulk thermoelectric materials with high figure of merit," Science **303**, 818–821 (2004).

[7] H. J. Wu, L.-D. Zhao, F. Zheng, D. Wu, Y. Pei, X. Tong, M. Kanatzidis, and J. Q. He, "Broad temperature plateau for thermoelectric figure of merit $zt > 2$ in phase-separated $pbte_{0.7}s_{0.3}$," Nat. Commun. **5**, 1–7 (2014).

[8] M. Hong, Z.-G. Chen, L. Yang, Y.-C. Zou, M. S. Dargusch, H. Wang, and J. Zou, "Realizing zt of 2.3 in $ge_{1-x-y}sb_xin_yte$ via reducing the phase-transition temperature and introducing resonant energy doping," Adv. Mater. **30**, 1705942 (2018).

[9] D. Wu, L. Xie, X. Xu, and J. He, "High thermoelectric performance achieved in gete?bi2te3 pseudo-binary via van der waals gap-induced hierarchical ferroelectric domain structure," Adv. Funct. Mater. **18**, 1806613 (2019).

[10] J. Li, X. Zhang, Z. Chen, S. Lin, W. Li, J. Shen, I. T. Witting, AlirezaFaghaninia, Y. Chen, A. Jain, L. Chen, G. J. Snyder, and YanzhongPei, "Low-symmetry rhombohedral gete thermoelectrics," Joule **2**, 976–987 (2018).

[11] B. Poudel, Q. Hao, Y. Ma, Y. Lan, A. Minnich, B. Yu, X. Yang, D. Wang, A. Muto, D. Vashaee, X. Chen, J. Liu, M. Dresselhaus, G. Chen, and Z. Ren, "High-thermoelectric performance of nanostructured bismuth

antimony telluride bulk alloys," Science **320**, 634–638 (2008).

[12] S. I. Kim, K. H. Lee, H. A. Mun, H. S. Kim, S. W. Hwang, J. W. Roh, D. J. Yang, W. H. Shin, X. S. Li, Y. H. Lee, G. J. Snyder, and S. W. Kim, "Dense dislocation arrays embedded in grain boundaries for high-performance bulk thermoelectrics," Science **348**, 109–114 (2015).

[13] L. Hu, H. Wu, T. Zhu, C. Fu, J. He, P. Ying, and X. Zhao, "Tuning multiscale microstructures to enhance thermoelectric performance of n-type bismuth-telluride-based solid solutions," Adv. Energy Mater. **5**, 1500411 (2015).

[14] J. Zhang, L. Song, S. H. Pedersen, H. Yin, L. T. Hung, and B. B. Iversen, "Discovery of high-performance low-cost n-type mg_3sb_2-based thermoelectric materials with multi-valley conduction bands," Nat. Commun. **8** (2017).

[15] M. Wood, J. J. Kuo, K. Imasato, and G. J. Snyder, "Improvement of low-temperature zt in a mg_3sb_2?mg_3bi_2 solid solution via mg-vapor annealing," Adv. Mater. **31** (2019).

[16] X. Shi, C. Sun, Z. Bu, X. Zhang, Y. Wu, S. Lin, W. Li, A. Faghaninia, A. Jain, and Y. Pei, "Revelation of inherently high mobility enables mg_3sb_2 as a sustainable alternative to n-bi_2te_3 thermoelectrics," Adv. Sci. **6** (2019).

[17] J. Mao, H. Zhu, Z. Ding, Z. Liu, G. Amila, Gamage, G. Chen, and Z. Ren, "High thermoelectric cooling performance of n-type mg_3bi_2-based materials," Science **365** (2019).

[18] L. E. Bell, "Cooling, heating, generating power, and recovering waste heat with thermoelectric systems," Science **321**, 1457–1461 (2008).

[19] J. He and T. M. Tritt, "Advances in thermoelectric materials research: Looking back and moving forward," Science **357**, 1–9 (2017).

[20] T. Tritt and M. Subramanian, "Thermoelectric materials, phenomena, and applications: a birds eye view," MRS Bulletin **31**, 188–198 (2006).

[21] J. Yang and T. Caillat, "Thermoelectric materials for space and automotive power generation," MRS Bulletin **31**, 224–229 (2006).

[22] J. Snyder and E. Toberer, "Complex thermoelectric materials," Nat. Mater. **7**, 105–114 (2008).

[23] J. R. Sootsman, D. Chung, and M. Kanatzidis, "New and old concepts in thermoelectric materials," Angew. Chem. **48**, 8616–8639 (2009).

[24] W. G. Zeier, A. Zevalkink, Z. M. Gibbs, G. Hautier, M. G. Kanatzidis, and G. J. Snyder, "Thinking like a chemist: Intuition in thermoelectric materials," Angew. Chem. **55**, 6826–6841 (2016).

[25] L.-D. Z. Xiao Zhang, "Thermoelectric materials: Energy conversion between heat and electricity," J. Materiomics. **1**, 92–105 (2015).

[26] T. Zhu, Y. Liu, C. Fu, J. P. Heremans, J. G. Snyder, and X. Zhao, "Compromise and synergy in high-efficiency thermoelectric materials," Adv. Mater. **29**, 1605884 (2017).

[27] J. Mao, Z. Liu, J. Zhou, H. Zhu, Q. Zhang, G. Chen, and Z. Ren, "Advances in thermoelectrics," Adv. in Phys. **67**, 69–147 (2018).

[28] Y. Pei, A. D. LaLonde, H. Wang, and G. J. Snyder, "Low effective mass leading to high thermoelectric performance," Energy Environ. Sci. **5**, 7963–7969 (2012).

[29] P. Gorai, V. Stevanović, and E. S. Toberer, "Computationally guided discovery of thermoelectric materials," Nat. Rev. Mater. **2**, 1–16 (2017).

[30] C. Fu, T. Zhu, Y. Pei, H. Xie, H. Wang, G. J. Snyder, Y. Liu, Y. Liu, and X. Zhao, "High band degeneracy contributes to high thermoelectric performance in p-type half-heusler compounds," Adv. Energy Mater. **4**, 1400600 (2014).

[31] Z. M. Gibbs, F. Ricci, G. Li, H. Zhu, K. Persson, G. Ceder, G. Hautier, A. Jain, and G. J. Snyder, "Effective mass and fermi surface complexity factor from ab initio band structure calculations," Comput. Mater. **3**, 1–7 (2017).

[32] J. Yan, P. Gorai, B. Ortiz, S. Miller, S. A. Barnett, T. Mason, V. Stevanović, and E. S. Toberer, "Material descriptors for predicting thermoelectric performance," Energy Environ. Sci. **8**, 983–994 (2015).

[33] J. Park, Y. Xia, and V. Ozoliņš, "High thermoelectric power factor and efficiency from a highly dispersive band in ba_2biau," Phys. Rev. Appl. **11**, 014058 (2019).

[34] J. He, M. Amsler, Y. Xia, S. S. Naghavi, V. Hegde, S. Hao, S. Goedecker, V. Ozoliņš, and C. Wolverton, "Ultralow thermal conductivity in full heusler semiconductors," Phys. Rev. Lett. **117**, 046602 (2016).

[35] P. Giannozzi, S. Baroni, N. Bonini, M. Calandra, R. Car, C. Cavazzoni, D. Ceresoli, G. L. Chiarotti, M. Cococcioni, I. Dabo, A. Dal Corso, S. de Gironcoli, S. Fabris, G. Fratesi, R. Gebauer, U. Gerstmann, C. Gougoussis, A. Kokalj, M. Lazzeri, L. Martin-Samos, N. Marzari, F. Mauri, R. Mazzarello, S. Paolini, A. Pasquarello, L. Paulatto, C. Sbraccia, S. Scandolo, G. Sclauzero, A. P. Seitsonen, A. Smogunov, P. Umari, and R. M. Wentzcovitch, "Quantum espresso: a modular and open-source software project for quantum simulations of materials," J. Phys. Condens. Matter , 395502 (19pp) (2009).

[36] P. Giannozzi, O. Andreussi, T. Brumme, O. Bunau, M. B. Nardelli, M. Calandra, R. Car, C. Cavazzoni, D. Ceresoli, and M. Cococcioni, "Advanced capabilities for materials modeling with quantum espresso," J. Phys. Condens. Matter , 465901 (31pp) (2017).

[37] D. R. Hamann, "Optimized norm-conserving vanderbilt pseudopotentials," Phys. Rev. B **88**, 085117 (2013).

[38] M. Schlipf and F. Gygi, "Optimization algorithm for the generation of {ONCV} pseudopotentials," Comput. Phys. Commun. **196**, 36–44 (2015).

[39] P. S. abd Marco Govoni, I. Hamada, and G. Galli, "Implementation and validation of fully relativistic GW calculations: Spinorbit coupling in molecules, nanocrystals, and solids," J. Chem. Theory Comput. **12**, 3523–3544 (2016).

[40] J. P. Perdew, K. Burke, and M. Ernzerhof, "Generalized gradient approximation made simple," Phys. Rev. Lett. **77**, 3865–3868 (1996).

[41] F. Tran and P. Blaha, "Accurate band gaps of semiconductors and insulators with a semilocal exchange-correlation potential," Phys. Rev. Lett. **102**, 226401 (2009).

[42] J. Heyd, G. E. Scuseria, and M. Ernzerhof, "Hybrid functionals based on a screened coulomb potential," J. Chem. Phys. **118**, 8207–8215 (2003).

[43] J. Heyd, G. E. Scuseria, and M. Ernzerhof, "Efficient hybrid density functional calculations in solids: Assessment of the heyd–scuseria–ernzerhof screened coulomb hybrid functional," J. Chem. Phys. **121**, 1187–1192 (2004).

[44] S. Poncé, G. Antonius, Y. Gillet, P. Boulanger, J. L. Janssen, A. Marini, M. Côté, and X. Gonze, "Temper-

ature dependence of electronic eigenenergies in the adiabatic harmonic approximation," Phys. Rev. B **90**, 214304 (2014).
[45] S. Poncé, Y. Gillet, J. L. Janssen, A. Marini, M. Verstraete, and X. Gonze, "Temperature dependence of the electronic structure of semiconductors and insulators," J. Chem. Phys. **143**, 1028137 (2015).
[46] F. Giustino, M. L. Cohen, and S. G. Louie, "Electron-phonon interaction using wannier functions," Phys. Rev. B **76**, 165108 (2007).
[47] J. Noffsinger, F. Giustino, B. D. Malone, C. H. Park, S. G. Louie, and M. L. Cohen, "Epw: A program for calculating the electron–phonon coupling using maximally localized wannier functions," Comput. Phys. Commun. **55**, 2140–2148 (2010).
[48] S. Ponce, E. R. Margine, C. Verdi, and F. Giustino, "Epw: Electron–phonon coupling, transport and superconducting properties using maximally localized wannier functions," Comput. Phys. Commun. **55**, 116–133 (2016).
[49] F. Giustino, "Electron-phonon interactions from first principles," Rev. Mod. Phys. **89**, 015003 (2017).
[50] N. Marzari and D. Vanderbilt, "Maximally localized generalized wannier functions for composite energy bands," Phys. Rev. B **56**, 12847–12865 (1997).
[51] I. Souza, N. Marzari, and D. Vanderbilt, "Maximally localized wannier functions for entangled energy bands," Phys. Rev. B **65**, 035109–1–13 (2001).
[52] A. A. Mostofi, J. R. Yates, Y.-S. Lee, I. Souza, D. Vanderbilt, and N. Marzari, "wannier90: A tool for obtaining maximally-localised wannier functions," Comput. Phys. Commun. **178**, 685–699 (2008).
[53] C. Verdi and F. Giustino, "Fröhlich electron-phonon vertex from first principles," Phys. Rev. Lett. **115**, 176401 (2015).
[54] S. materials to the main text, for computational details on electron-phonon scattering, phase stability and defects..
[55] G. K. Madsen and D. J. Singh, "Boltztrap. a code for calculating band-structure dependent quantities," Comput. Phys. Commun. **175**, 67–71 (2006).
[56] Q. Song, T.-H. Liu, J. Zhou, Z. Ding, and G. Chen, "*Ab initio* study of electron mean free paths and thermoelectric properties of lead telluride," Mater. Today Phys. **2**, 69–77 (2017).
[57] J. Cao, J. D. Querales-Flores, A. R. Murphy, S. Fahy, and I. Savić, "Dominant electron-phonon scattering mechanisms in n-type pbte from first principles," Phys. Rev. B **98**, 205202 (2018).
[58] J. Zhou, H. Zhu, T. Liu, Q. Song, R. He, J. Mao, Z. Liu, W. Ren, B. Liao, D. J. Singh, and G. Chen, "Large thermoelectric power factor from crystal symmetry-protected non-bonding orbital in half-heuslers $nb_{1-x}ti_xfesb$," Nat. Commun. **9**, 1–9 (2018).
[59] Y. Xia, J. Park, F. Zhou, and V. Ozoliņš, "High thermoelectric power factor in intermetallic cosi arising from energy filtering of electrons by phonon scattering," Phys. Rev. Appl. **11**, 024017 (2019).
[60] A. Jain, S. P. Ong, G. Hautier, W. Chen, W. D. Richards, S. Dacek, S. Cholia, D. Gunter, D. Skinner, G. Ceder, and K. A. Perssson, "Commentary: The materials project: A materials genome approach to accelerating materials innovation," APL Mater. **1**, 1002 (2013).
[61] G. Bergerhoff and I. D. Brown, "Inorganic crystal structure database," Crystallographic Databases , 77–95 (1987).
[62] A. Belsky, M. Hellenbrandt, V. L. Karen, and P. Luksch, "New developments in the inorganic crystal structure database (icsd): accessibility in support of materials research and design," Acta Crystallogr. B **58**, 364–369 (2002).
[63] M. Hellenbrandt, "The inorganic crystal structure databae (icsd) – present and future," Crystallogr. Rev. **10**, 17–22 (2004).
[64] G. Kresse and J. Hafner, "*Ab initio* molecular dynamics for liquid metals," Phys. Rev. B **47**, 558–561 (1993).
[65] G. Kresse and J. Hafner, "*Ab initio* molecular-dynamics simulation of the liquid-metal˘amorphous-semiconductor transition in germanium," Phys. Rev. B **49**, 14251–14269 (1994).
[66] G. Kresse and J. Furthmüller, "Efficiency of ab-initio total energy calculations for metals and semiconductors using a plane-wave basis set," Comput. Mater. Sci. **6**, 15–50 (1996).
[67] G. Kresse and J. Furthmüller, "Efficient iterative schemes for *ab initio* total-energy calculations using a plane-wave basis set," Phys. Rev. B **54**, 11169–11186 (1996).
[68] P. E. Blöchl, "Projector augmented-wave method," Phys. Rev. B **50**, 17953–17979 (1994).
[69] M. Methfessel and A. Paxton, "High-precision sampling for brillouin-zone integration in metals," Phys. Rev. B **40**, 3616–3621 (1989).
[70] G. Makov and M. C. Payne, "Periodic boundary conditions in *ab initio* calculations," Phys. Rev. B **51**, 074014 (1995).
[71] C. Freysoldt, J. Neugebauer, and C. G. V. de Walle, "Fully *Ab Initio* finite-size corrections for charged-defect supercell calculations," Phys. Rev. B **102**, 016402 (2009).
[72] C. Freysoldt, J. Neugebauer, and C. G. V. de Walle, "Electrostatic interactions between charged defects in supercells," Phys. Stat. Solid. **248**, 1067 (2011).
[73] S. Lany and A. Zunger, "Assessment of correction methods for the band-gap problem and for finite-size effects in supercell defect calculations: Case studies for zno and gaas," Phys. Rev. B **78**, 235104 (2008).
[74] A. Alkauskas, P. Broqvist, and A. Pasquarello, "Defect energy levels in density functional calculations: Alignment and band gap problem," Phys. Rev. B **101**, 046404 (2008).
[75] H.-P. Komsa, P. Broqvist, and A. Pasquarello, "Alignment of defect levels and band edges through hybrid functionals: Effect of screening in the exchange term," Phys. Rev. B **81**, 205118 (2010).
[76] H.-P. Komsa and A. Pasquarello, "Assessing the accuracy of hybrid functionals in the determination of defect levels: Application to the as antisite in gaas," Phys. Rev. B **84**, 075207 (2011).
[77] A. Alkauskas and A. Pasquarello, "Band-edge problem in the theoretical determination of defect energy levels: The o vacancy in zno as a benchmark case," Phys. Rev. B **84**, 125206 (2011).
[78] M.-H. Du, "Density functional calculations of native defects in $ch_3nh_3pbi_3$: Effects of spin-orbit coupling and self-interaction error," J. Phys. Chem. Lett. **6**, 1461–1466 (2015).
[79] R. He, D. Kraemer, J. Mao, L. Zeng, Q. Jie, Y. Lan, C. Lie, J. Shuai, H. S. Kim, Y. Liu, D. Broido, C.-W. Chu, G. Chen, and Z. Ren, "Achieving high power factor and output power density in p-type half-heuslers

$nb_{1-x}ti_xfesb$," Proc. Natl. Acad. Sci. **113**, 13576–13581 (2016).

[80] J. R. Sootsman, H. Kong, C. Uher, J. J. D. Angelo, C.-I. Wu, T. P. Hogan, T. Caillat, and M. G. Kanatzidis, "Large enhancements in the thermoelectric power factor of bulk pbte at high temperature by synergistic nanostructuring," Angew. Chem. **47**, 8618–8622 (2008).

[81] Y. Pei, S. Xiaoya, L. Aaron, L. C. H. Wang, and G. Snyder, "Convergence of electronic bands for high performance bulk thermoelectrics," Nature **473**, 66–69 (2011).

[82] Y. Pei, H. Wang, and G. Snyder, "Band engineering of thermoelectric materials," Adv. Mater. **24**, 6125–6135 (2012).

[83] K. Biswas, J. He, I. D. Blum, C.-I. Wu, T. P. Hogan, D. N. S. abd Vinayak P. Dravid, and M. G. Kanatzidis, "High-performance bulk thermoelectrics with all-scale hierarchical architectures," Nature **489**, 414–418 (2012).

[84] G. E. Smith and R. Wolfe, "Thermoelectric properties of bismuth- antimony alloys," J. Appl. Phys. **33**, 841–846 (1962).

[85] G. S. Nolas, J. Sharp, and H. J. Goldsmid, *Thermoelectrics* (Springer, 2001).

[86] F. Zhou, W. Nielson, Y. Xia, and V. Ozoliņš, "Lattice anharmonicity and thermal conductivity from compressive sensing of first-principles calculations," Phys. Rev. Lett. **113**, 185501 (2014).

[87] W. Li, J. Carrete, N. A. Katcho, and N. Mingo, "Shengbte: A solver of the boltzmann transport equation for phonons," Comput. Phys. Commun. **185**, 1747–1758 (2014).

[88] A. Zunger, "Beware of plausible predictions of fantasy materials," Nature **566**, 447–449 (2019).

[89] N. V, T. J. Burch, K. Rag, and J. . Budnick, "Rmx compounds fromed by alkaline earths, europium and ytterbium - i. ternary phases with m = cu, ag, au; x= sb, bi," J. Less Common Met. **166**, 319–327 (1990).